Scientific Research Publishing

Journal of Flow Control, Measurement & Visualization, 2023, 11, 30-48
https://www.scirp.org/journal/jfcmv
ISSN Online: 2329-3330
ISSN Print: 2329-3322

Numerical Study on Low-Reynolds Compressible Flows around Mars Helicopter Rotor Blade Airfoil

Takuma Yamaguchi, Masayuki Anyoji

Interdisciplinary Graduate School of Engineering Sciences, Kyushu University, Fukuoka, Japan
Email: yamaguchi.takuma.097@s.kyushu-u.ac.jp, anyoji.masayuki.660@m.kyushu-u.ac.jp

How to cite this paper: Yamaguchi, T. and Anyoji, M. (2023) Numerical Study on Low-Reynolds Compressible Flows around Mars Helicopter Rotor Blade Airfoil. *Journal of Flow Control, Measurement & Visualization*, **11**, 30-48.
https://doi.org/10.4236/jfcmv.2023.112003

Received: November 18, 2023
Accepted: April 25, 2023
Published: April 28, 2023

Abstract

High-speed rotor rotation under the low-density condition creates a special low-Reynolds compressible flow around the rotor blade airfoil where the compressibility effect on the laminar separated shear layer occurs. However, the compressibility effect and shock wave generation associated with the increase in the Mach number (M) and the trend change due to their interference have not been clarified. The purpose is to clear the compressibility effect and its impact of shock wave generation on the flow field and aerodynamics. Therefore, we perform a two-dimensional unsteady calculation by Computational fluid dynamics (CFD) analysis using the CLF5605 airfoil used in the Mars helicopter Ingenuity, which succeeded in its first flight on Mars. The calculation conditions are set to the Reynolds number (Re) at 75% rotor span in hovering (Re = 15,400), and the Mach number was varied from incompressible (M = 0.2) to transonic (M = 1.2). The compressible fluid dynamics solver FaSTAR developed by the Japan aerospace exploration agency (JAXA) is used, and calculations are performed under multiple conditions in which the Mach number and angle of attack (α) are swept. The results show that a flow field is similar to that in the Earth's atmosphere above M = 1.0, such as bow shock at the leading edge, whereas multiple λ-type shock waves are observed over the separated shear layer above $\alpha = 3^\circ$ at M = 0.80. However, no significant difference is found in the C_p distribution around the airfoil between M = 0.6 and M = 0.8. From the results, it is found that multiple λ-type shock waves have no significant effect on the airfoil surface pressure distribution, the separated shear layer effect is dominant in the surface pressure change and aerodynamic characteristics.

Keywords

CFD, CLF5605 Rotor Blade Airfoil, Compressibility Effect, Low-Reynolds

Number, Mars Helicopter, Separation Bubble, Shock Wave

1. Introduction

In recent years, the Mars Helicopter (MH) has been developed as a new means of exploring the planet Mars in conjunction with a rover mission. The MH is characterized by its ability to move at relatively high speeds, unaffected by the complex terrain of the Martian surface which is inaccessible to rovers. Cooperation with the rover is expected to extend its exploration range in acquiring detailed and meaningful scientific data from areas that have been previously difficult to explore. Proposed Martian helicopters include the Martian Autonomous Rotary-Wing Vehicle (MARV) from the University of Maryland [1], the Hex-Acopter for Martian pItcrater exploraTiON (HAMILTON) [2] [3] which is being studied mainly by the JAXA, and "Ingenuity" designed by the National Aeronautics and Space Administration (NASA) Jet Propulsion Laboratory (JPL). Among these, Ingenuity completed the first successful powered flight on a planet other than Earth [4] during its first flight on Mars in April 2021 in a mission called "Mars 2020". However, since the current Ingenuity is positioned as a technology demonstrator, it has only minimum performance for near-surface flight. In particular, for future practical flight exploration over a wide area, improvement of aerodynamic performance is an essential technical challenge to enable increased payload capacity and longer cruising range.

Table 1 compares atmospheric conditions on Earth and Mars [5]. Since Mars has about 40% gravity and an atmospheric density of about 1% compared to that of Earth, these characteristics make it a harsh rarefied environment for the MH. In addition, the speed of sound on Mars is about 70% that of Earth because the atmosphere is mainly composed of CO_2 and the average temperature is low at approximately 223.2˚C. As a result, the Reynolds number (Re) in the flow around the MH rotor blade becomes low at $Re = O(10^3 - 10^4)$ and the Mach number (M) reaches nearly $M = 0.80$ where shock waves are more likely to occur, especially near the blade tips. Figure 1 shows flow conditions around the

Table 1. Mars atmospheric condition [5].

Physical properties	Earth	Mars
Density, ρ [kg/m^3]	1.225	0.017
Temperature, T [K]	288.2	223.2
Gas constant, R [J/kg·K]	287.1	188.9
Specific heat ratio, γ	1.400	1.289
Dynamic viscosity, μ [Pa·s]	1.750×10^{-5}	1.130×10^{-5}
Static pressure, p [kPa]	101.3	0.720
Sound speed, a [m/s]	340.4	233.1

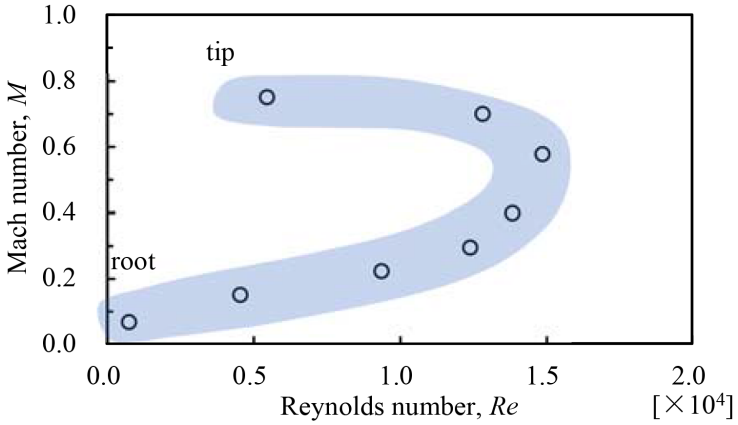

Figure 1. Flow conditions around the rotor of "ingenuity" in hovering (created based on [6]).

rotor blade of Ingenuity [6].

Such low-Reynolds-number compressible flow is a very specific flow condition for the aerodynamic design of airfoils. Several studies have been reported on the flow fields around the airfoils under these special flow conditions [7]-[14]. Canuto *et al.* [7] investigated the compressibility effect around a cylinder in the low Reynolds number region using direct numerical simulation (DNS). They reported that the compressibility effect elongates the wake and causes a slight delay in separation. Anyoji *et al.* [11] investigated the effect of compressibility at Re = 11,000 using NACA0012-34 airfoil in the Mars Wind Tunnel (MWT) at Tohoku University. They revealed that the lift coefficient decreased with an increasing Mach number in the high angles of attack above $\alpha = 7^{\circ}$. This is because the compressibility effect delays the flow separation and laminar-to-turbulent transition, preventing the laminar separation bubble (LSB) formation. Meanwhile, Mukohara *et al.* [12] investigated the compressibility effect on a leading-edge LSB on a flat plate at Re = 6100 and 11,000. Their results showed that the rolled-up separated shear layer due to the Kelvin-Helmholtz (KH) instability is stabilized by the compressibility effect, delaying the laminar-to-turbulent transition and reattachment. The magnitude of this effect is more remarkable as the Reynolds number is higher. However, these studies have been limited to M = 0.80 or less, partly because it is difficult to conduct low-Reynolds number and transonic wind tunnel tests. Therefore, the details of the flow field at transonic speeds such as the compressibility effect on the interference between the LSB and shock waves, remain unknown. Drela [13] numerically investigated a shock/boundary layer interaction around the Eppler 387 airfoil at Re = 200,000 which is one order of magnitude larger than the target Reynolds numbers. He successfully captured the generation of the multiple λ-type shock waves over the separation bubble at M = 0.65. However, the laminar separation does not occur at these relatively high Reynolds numbers which correspond to the turbulent boundary layer region. The lift-to-drag ratio deteriorates sharply below Re = 70,000 due to the boundary layer transition (**Figure 2**) [14]. In other words, the

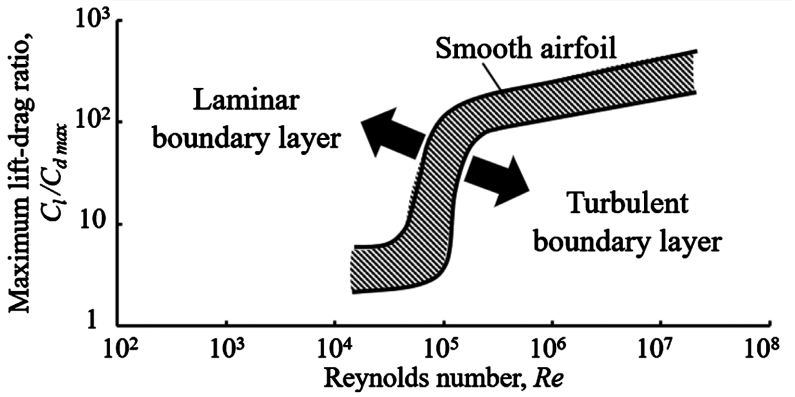

Figure 2. Dependence of Reynolds number (*Re*) of maximum lift-drag ratio (created based on [14]).

flow field is expected to be different at the flight Reynolds numbers of the MH. Meanwhile, Sato *et al.* performed CFD simulations of the three-dimensional rotor blade of Ingenuity using the CLF5605 airfoil to investigate the presence and effects of shock wave generation [3]. The results showed that even at a high Mach number at the wing tip, M_{tip} = 0.90, no shock waves are generated in the Martian atmosphere, and no deterioration in the aerodynamic performance occurs. This is because the blade tip vortex generated by the front blade induces a flow in the rotational direction, which reduces the local Mach number around the blade. Although no shock waves were observed in the flow field below M_{tip} = 0.90 in their study, it is assumed that for future practical operation of the MH, it will be required to fly at higher rotational speeds to increase payload capacity and extend the cruising range.

In response to such requirements, there is an insufficient basic understanding of the details of the fluid structure, such as the LSB/shock interaction when shock waves are generated, and their effects on the aerodynamic performance. This paper describes the compressibility effect and its impact of shock wave generation on the flow field and aerodynamics by varying the angles of attack and the rotational speed (Mach number) from incompressible to transonic speeds using the CLF5605 airfoil. Because of the high computational cost of three-dimensional calculations and the impracticality of conducting a large number of calculation cases, the flow field around the two-dimensional airfoil is simulated.

First, comparisons with previous studies and confirmation of the grid convergence were conducted as validation and verification of our computational method. Next, the compressible effect was investigated by comparing the flow field at M = 0.2, which corresponds to an incompressible flow, with that at M = 0.6, which is a compressible flow with no shock waves on the upper surface. Finally, the Mach number was increased in 0.2 steps from 0.6 to investigate the effect of the shock wave generation. This section describes the research background and purpose. Section 2 explains the computational setup. The computational results and discussion are given in section 3. Section 4 summarizes the results, including future works.

2. Computational Setup

2.1. Computational Model and Flow Condition

The CLF5605 is used as the target airfoil which has been adopted as the airfoil for the rotor blades of Ingenuity. Its geometric shape is shown in Figure 3. The CLF5605 is characterized by its thinness, small leading-edge radius, and large camber which has a maximum thickness ratio of 5.0% to the chord length (c) at $x/c = 0.20$ and a maximum camber ratio of 4.9% at $x/c = 0.59$.

For the aerodynamic design of Ingenuity's rotor blades, Koning *et al.* [6] have investigated the two-dimensional (2D) flow field around the CLF5605 at Re = 15,400 and M = 0.60 by CFD. This study simulates the flows corresponding to the equivalent chord (r/R = 0.75) of the Ingenuity rotor blades. Table 2 shows the set flow conditions. As conducted by Koning *et al.* [6], the base case in this study is defined as Re = 15,400 and M = 0.60 which is compared with the CFD results for validation. However, there is no wind tunnel that can realize these conditions, and it is difficult to conduct a wind tunnel test. Therefore, we investigated it by numerical calculation. Note that the Mars wind tunnel [15] that can achieve low-Reynolds-number compressible flows close to the flow conditions shown in Table 2 has been developed. However, even with such a special wind tunnel for Martian atmospheric flight, it is difficult to directly compare our calculations with experimental results because the relevant flow conditions are outside the operational envelope. Therefore, we evaluate the validity by comparing our results with the numerical results of Koning *et al.* [6]. Details are discussed in subsection 2.4.

Since this study focuses on the separated shear layer compressibility effects in

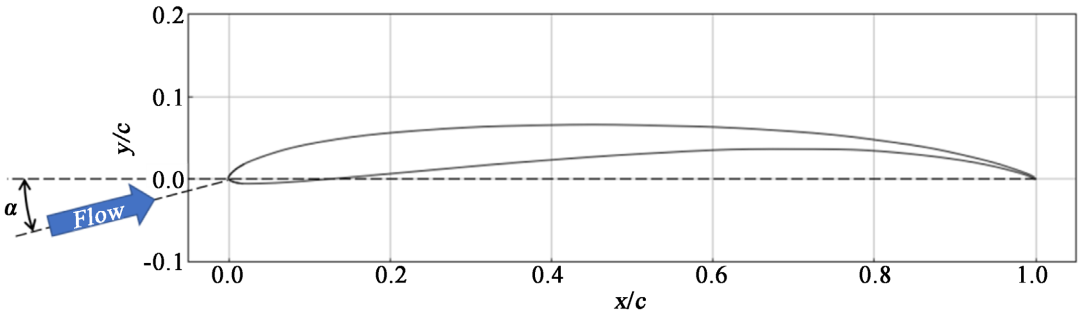

Figure 3. CLF5605 airfoil used for rotor blade of Ingenuity.

Table 2. Flow condition.

Physical properties	Value
Reynolds number, Re	15,400
Mach number, M	0.20, 0.60, 0.80, 1.0, 1.2
The angle of attack, α°	0 to 10 (in increments of 1˚)
Prandtl number	0.71
Turbulent Prandtl number	0.90

the low *Re* regime, especially pure *M* effects on shock wave interference, the *Re* is fixed and only the *M* is varied. Therefore, the *M* effect on the flow field and the aerodynamic characteristics were evaluated by varying the *M* while keeping *Re* = 15,400. In the actual operation of the MH, however, the *Re* also changes as the rotor speed (Mach number) is varied. A computational grid was used with a fixed chord length of 1.0 m in all cases. The *Re* and *M* were set by changing the density and static pressure as shown below:

$$\rho = \frac{Re \cdot \mu}{Uc} = \frac{Re \cdot \mu}{M\sqrt{\gamma RT}c} \tag{1}$$

$$p = \rho RT = \frac{Re \cdot \mu}{M}\sqrt{\frac{RT}{\gamma}} \tag{2}$$

In the base case, from Equations (1) and (2), the density and pressure are $\rho = 1.24 \times 10^{-3}\ \mathrm{kg/m^3}$ and $p = 52.5\ \mathrm{Pa}$, respectively. The (turbulent) Prandtl number was assumed to be the same as that of air according to the flow condition by Koning *et al.* [6].

2.2. Computational Methods

Two-dimensional unsteady calculations were performed using FaSTAR [16], a compressible fluid dynamics solver developed by JAXA. **Table 3** compares the methods used in this study with those used by Koning *et al.* [6]. Their computational method is followed in this study. The governing equation is shown below:

$$\frac{\partial}{\partial t}\int_V Q\mathrm{d}v + \int_S \left[F(Q) - \frac{1}{Re}F_v(Q)\right]\cdot \mathrm{d}s = 0 \tag{3}$$

where Q is the conserved vector, F is the inviscid vector, F_v is the viscous vector, and ds is the outward normal vector for each cell with the absolute value of the surface area. The governing equation was discretized by the finite volume method while SLAU2 was used to calculate the inviscid flux [17]. Since SLAU2 is reported to be very robust against shock wave anomalies [17], it can be systematically and efficiently calculated for a wide range of Mach numbers and angle of attack conditions without changing the method. It has also been reported that turbulence models and transition models are effective for capturing laminar separation bubbles (LSBs) on the airfoil surface [18] [19]. Based on these, the

Table 3. Computational methods.

	Koning *et al.* [6]	Current study
CFD solver	OVERFLOW 2.2n	FaSTAR [16]
Inviscid flux	6th-order central difference	SLAU2 [17]
Time marching	2nd-order backward difference	LU-SGS [23]
Gradient calculation	N/A	GLSQ [24]
Flux limiter	N/A	Minmod [25]
Turbulence model	SA-AFT2017b [19]	Menter SST with γ-$Re_{\theta t}$ [21] [22]

turbulence and transition model SA-AFT2017b [20] was employed in the study by Koning *et al.* [6] In this study, Menter SST was used as the turbulence model [21] with Menter γ-$Re_{\theta t}$ as the transition model [22].

2.3. Computational Grid

Figure 4 shows the overall view of the calculation grid and an enlarged view around the airfoil. This study adopted an *O*-shaped grid which has a small change in the grid density even when the angle of attack is changed. The calculation area was set to 100*c* and the first layer thickness width was determined so that y^+ calculated would be less than 1.0 under all flow conditions. To evaluate the grid level effect on aerodynamic performance, three levels of mesh refinement (coarse, medium, and fine) were conducted. Based on the medium mesh with 124,000 grid points, the fine (163,800 points) and coarse (59,400 points) mesh were created by increasing or decreasing the number of grid points in the circumferential and vertical directions of the airfoil, respectively.

2.4. Validation & Verification

Since there is no experimental data under the relevant flow conditions, the qualitative validity of the results was evaluated by comparing them with those of Koning *et al.* [6]. **Figure 5** compares the present results for the aerodynamic coefficients (C_l, C_d) at Re = 15,400 and M = 0.60 with those of Koning *et al.* [6].

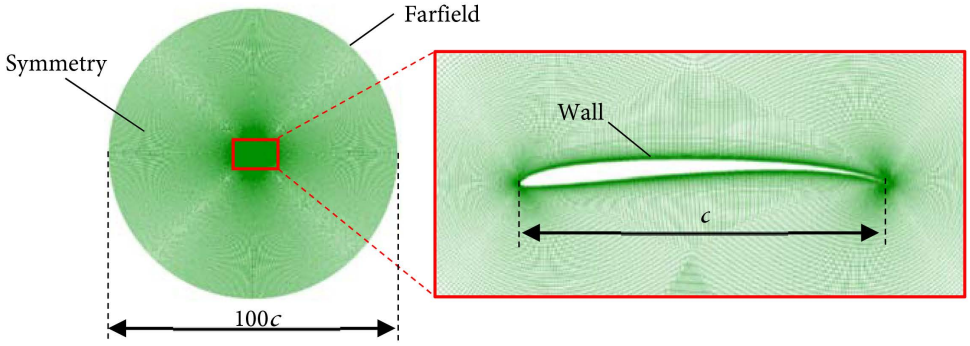

Figure 4. Overall and enlarged views of medium grid.

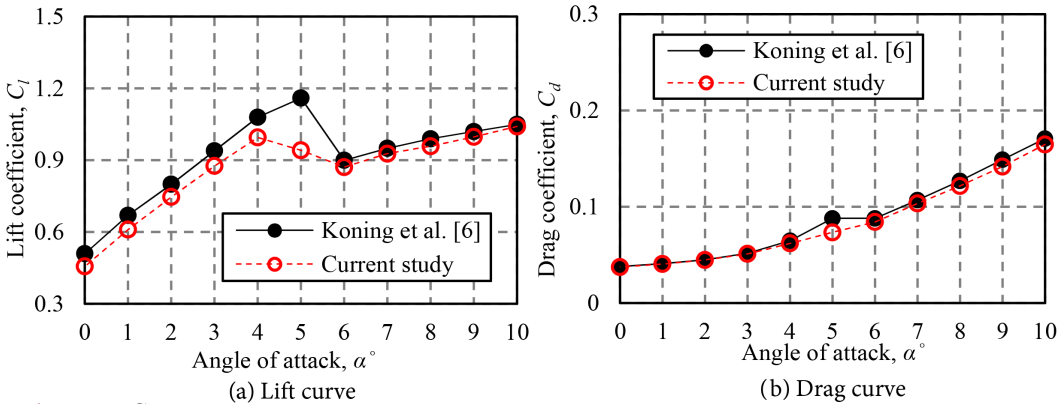

Figure 5. Comparison of aerodynamic coefficients at Re = 15,400 and M = 0.60.

Figure 6 shows the time history of the aerodynamic coefficients at $\alpha = 6^\circ$ as a typical case. Since the convergence is observed after the dimensionless time (ut/c) of 50 for all angles of attack, the aerodynamic coefficients shown in Figure 5 are averaged from 50 to 60 in the dimensionless time. From Figure 5, although both the lift and drag coefficients agree over a wide range of angles of attack, the maximum difference is about 19% for C_l and about 16% for C_d at $\alpha = 5^\circ$. Also, the lift coefficient of the present study is approximately 8% smaller than that of Koning *et al.* below $\alpha = 4^\circ$. These differences can be attributed primarily to the relatively early flow separation in the present CFD. In addition, in a previous study [26] that compared the results of wind tunnel tests and Reynolds-averaged Navier-Stokes (RANS) simulations of Mars aircraft in the low Reynolds number region, C_l measured by RANS was about 7 to 10% lower than the results of wind tunnel tests. It is reported that this is due to the limitation of separation prediction by the turbulence model. Since the same turbulence model (Menter SST and γ-$Re_{\theta t}$) is also used in this study, it is considered that the difference from Koning *et al.*'s study [6] was due to the error in separation prediction. The details of the flow field in the base case are described in Section 3.1. Although the above differences are observed, these do not interfere with the qualitative discussion of the flow field around the airfoil as the angle of attack increases. Hence, the same computational method was employed for the subsequent calculations.

Figure 7 compares the aerodynamic coefficients for the base case ($Re = 15{,}400$ and $M = 0.60$) at three different grid levels. Since the convergence was observed after dimensionless time 50 for all computational grid cases, Figure 7 shows the

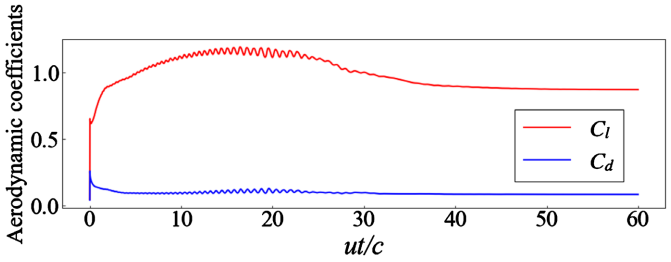

Figure 6. Time history of aerodynamic coefficients at $\alpha = 6^\circ$.

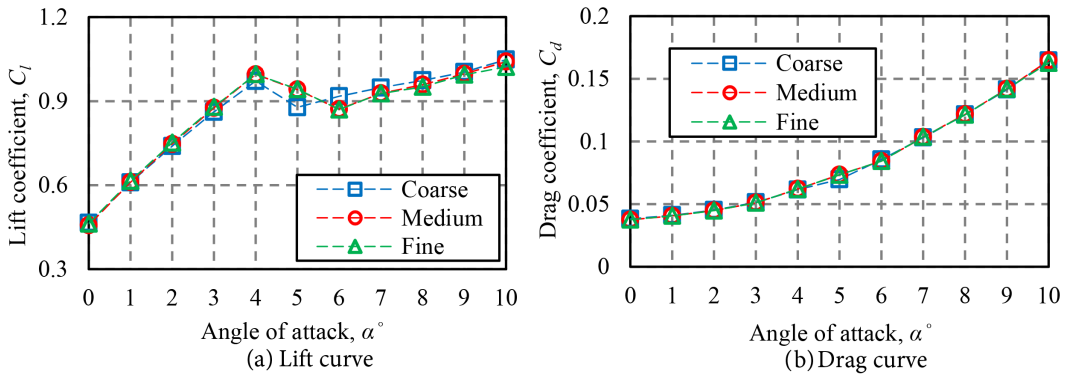

Figure 7. Comparison of aerodynamic coefficients at $Re = 15{,}400$ and $M = 0.60$ using grids with three different grid densities.

averaged value from the dimensionless time of 50 to 60. As shown in Figure 7, similar aerodynamic coefficients are obtained at each grid level, although there are slight differences at $\alpha = 5^\circ$ and 6˚, respectively. In particular, comparing the medium and coarse grids at $\alpha = 5^\circ$, the differences in lift and drag coefficients were approximately 7% and 5%, respectively. In contrast, the difference between the medium and fine grids was less than 2% for both the lift and drag coefficients at all angles of attack. From this result, it was judged that the medium grid converged sufficiently, and the medium grid (124,000 points) was used for all calculations.

3. Results and Discussions

3.1. Flow Field around CLF5605 Airfoil

Figure 8 and Figure 9 show the averaged flow fields of the base case (Re = 15,400 and M = 0.60) and the pressure coefficient (C_p) on the airfoil surface, respectively. Figure 10 indicates the separation locations calculated based on the skin-friction vectors in the x direction (C_{fx}) on the airfoil surface. For reference, Figure 11 shows the pressure coefficient distribution on the suction side of the flat plate with a typical LSB [11]. Figure 11 suggests that a laminar separation occurs on the suction side and the separated shear layer reattaches near the trailing edge, resulting in the formation of the LSB. However, a comparison of Figure 9 and Figure 11 suggests there is no clear pressure recovery indicating a laminar-to-turbulent transition and the C_p at the trailing edge is not near zero but about −0.5, indicating a separated flow without reattachment. Although a recirculation region is observed near the trailing edge in Figure 8, it seems to be forcibly reattached near the trailing edge due to the large reversed flow. These are thought to be due to the dependence of the turbulence model on the turbulent transition and the fact that the recirculation region is somewhat overestimated because of the two-dimensional calculation. As described above, it is debatable whether or not the separated flow reattaches at the trailing edge. However, in light of past findings based on the C_p distributions, it is natural to assume that the separated flow without reattachment occurs on the suction side.

Based on this assumption, a gradual shift can be found from the trailing-edge separation flow to the leading-edge separation flow as the angle of attack increases. Especially between $\alpha = 3^\circ$ and 5˚, when the separation point moves dramatically forward, most of the upper surface is covered by the separated flow at $\alpha = 5^\circ$ or more. The drop in the C_l at $\alpha = 5^\circ$ shown in Figure 5 can be attributed to this change in the leading-edge separation flow. Between $\alpha = 4^\circ$ and 6˚, the C_p distributions on the pressure side and the suction side from the leading edge to the suction peak hardly change while the C_l decreases with a slight pressure change after the suction peak. At $\alpha \geq 6^\circ$, the negative pressure in the suction peak increases and the positive pressure on the pressure side also increases, resulting in an increase in the C_l as the angle of attack increases.

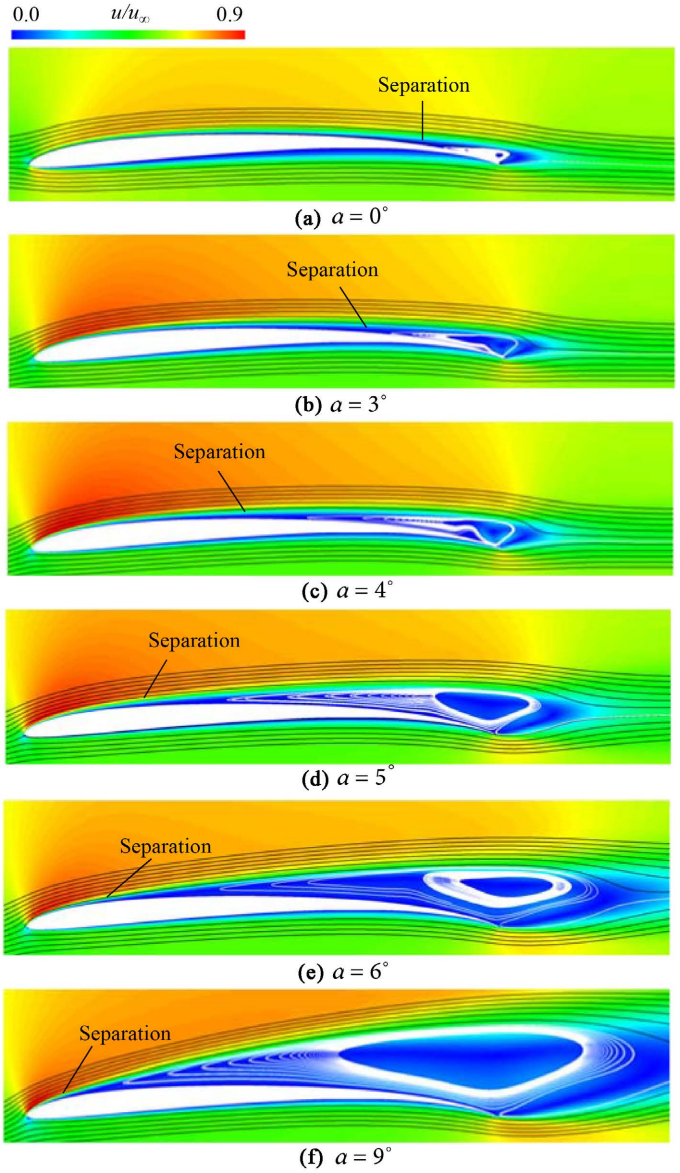

Figure 8. Averaged velocity fields and streamlines around CLF5605 at Re = 15,400 and M = 0.60.

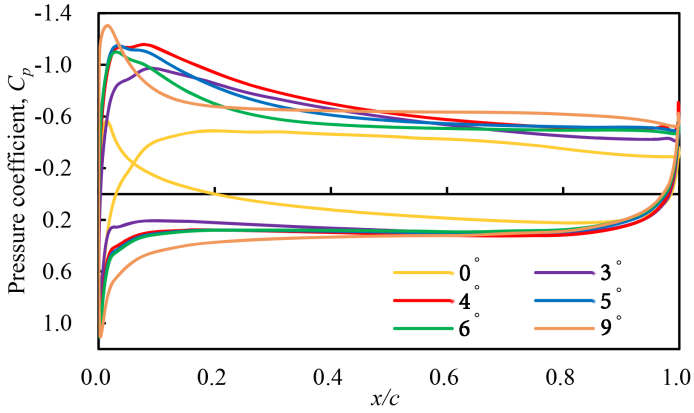

Figure 9. Pressure coefficient distribution.

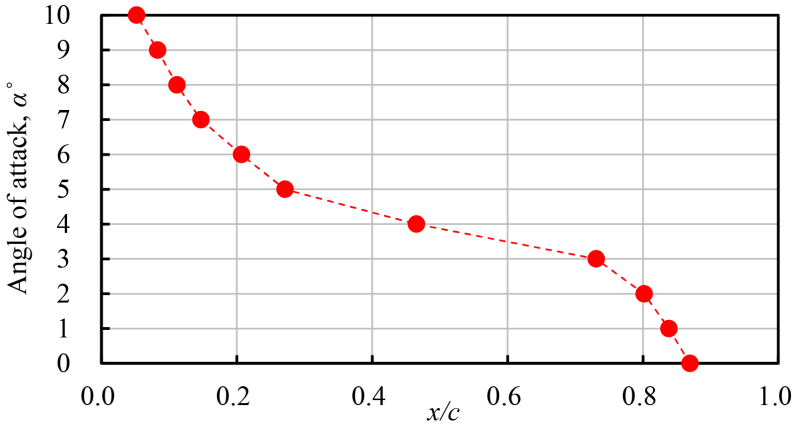

Figure 10. Separation locations for base case.

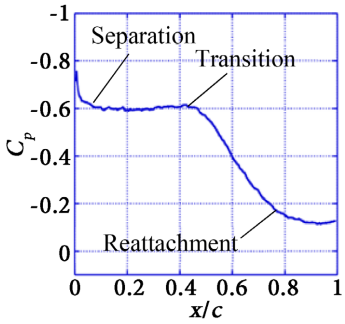

Figure 11. Typical C_p distribution on flat plate with leading-edge separation bubble at Re = 11,000 and M = 0.60 for α = 3˚ [11].

3.2. Mach Number Effect

3.2.1. Compressibility Effect

To evaluate the compressibility effect on aerodynamic performance and the flow fields, the results for M = 0.20 and M = 0.60 are compared as representatives of the incompressible and compressible flows, respectively. **Figure 12** and **Figure 13** show the lift and drag curves as well as the ratio of the difference in pressure drag to the difference in total drag, respectively. Meanwhile, **Figure 14** compares the C_p distributions for M = 0.20 and M = 0.60. The C_l below α = 4˚ increases almost linearly with increasing the angle of attack for both M. The characteristics of the C_p distribution shown in **Figure 14(a)**, especially the fact that the C_p does not recover to zero at the trailing edge, indicate a common trailing edge separation flow in both cases. Since there is little difference in the C_p distribution on the pressure side, the difference in the C_l below α = 4˚ is attributed to the difference in the negative pressure level on the suction surface. As explained above, the C_l drop is observed at α = 5˚ for M = 0.60 whereas it increases with the angle of attack for M = 0.20 up to α = 10˚ without the lift drop. The result is the C_l at M = 0.20 exceeds that at M = 0.60 above α = 5˚. In particular, a nonlinear lift increase is confirmed between α = 6˚ to 7˚. The C_p distributions shown in **Figure 14(b)** and **Figure 14(c)** suggest that this nonlinear lift increase at M = 0.20 is due to the increase in the negative pressure level on the suction side by the

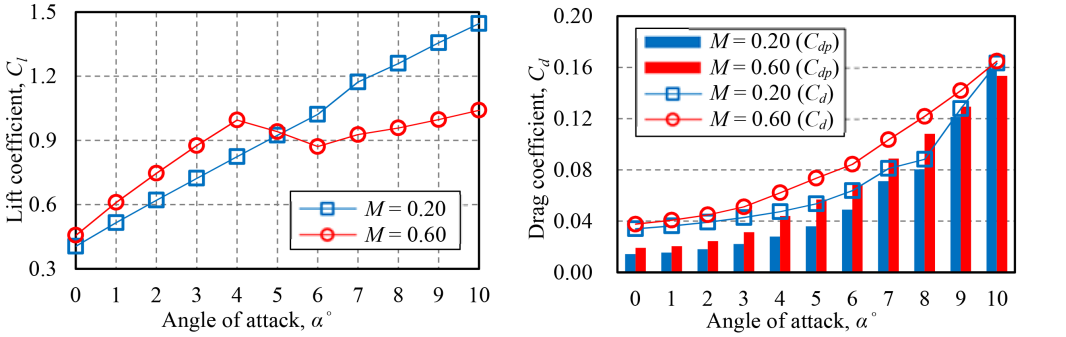

(a) Lift curve (b) Drag curve and pressure drag coefficients (C_{dp})

Figure 12. Comparison of the aerodynamic coefficients at $M = 0.20$ and 0.60.

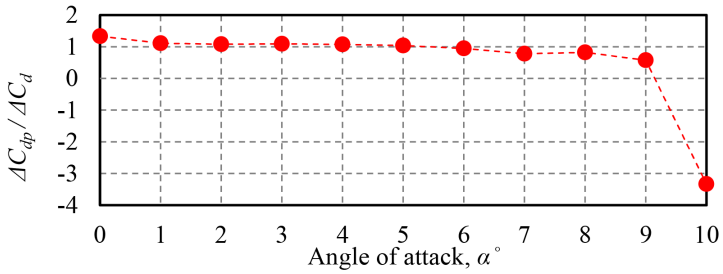

Figure 13. Ratio of difference in pressure drag $\Delta C_{dp}\left(=C_{dp_{M=0.6}}-C_{dp_{M=0.2}}\right)$ to difference in total drag $\Delta C_d\left(=C_{d_{M=0.6}}-C_{d_{M=0.2}}\right)$.

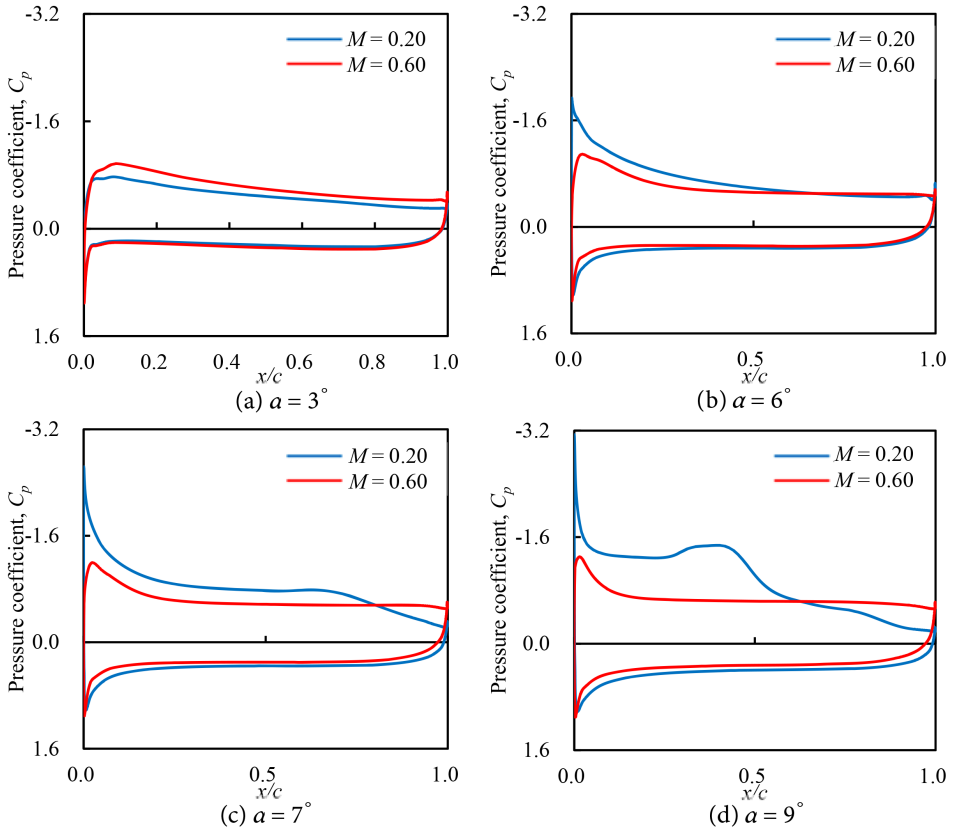

Figure 14. Comparison of the pressure coefficient distribution.

formation of LSB. The averaged flow field at $\alpha = 7^\circ$ shown in Figure 15 also indicates the formation of LSB near the center on the suction side.

In contrast to the C_l characteristics described above, Figure 12(b) indicates a larger drag coefficient at $M = 0.60$ for most angles of attack. Figure 16 compares the locations of the separation and reattachment for each M. These locations are also determined from the skin frictional vector as shown in Figure 10. The flow separation commonly occurs for all M, especially below $\alpha = 6^\circ$ when the flow

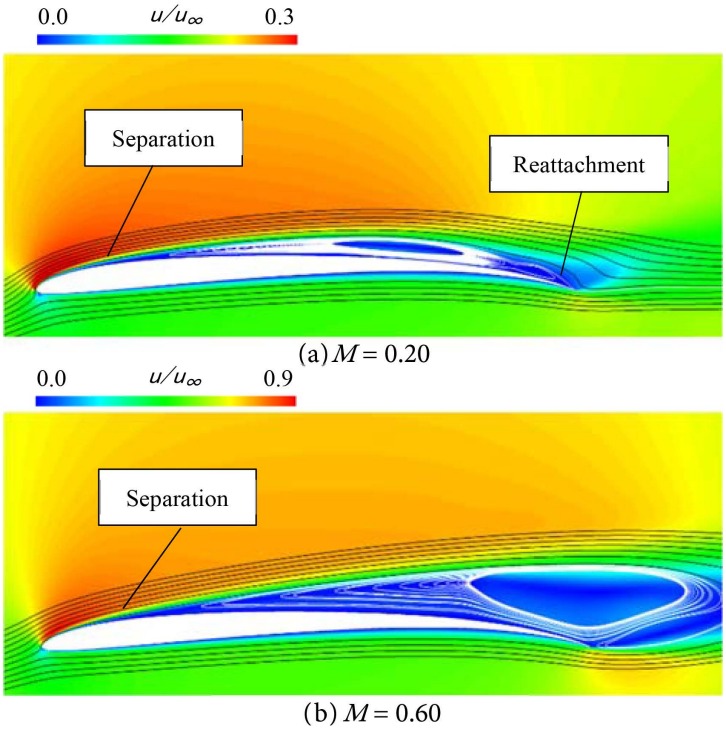

Figure 15. Averaged velocity fields and streamlines at $\alpha = 7^\circ$.

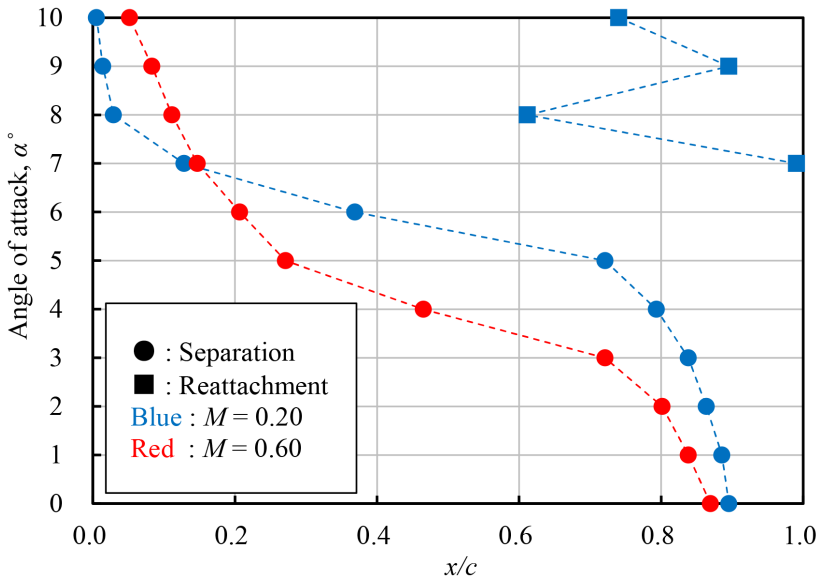

Figure 16. Compressibility effect on separation and reattachment locations.

separates more upstream at $M = 0.60$. However, above $\alpha = 7^{\circ}$, the LSB forms only at $M = 0.20$ and the flow separation occurs more upstream near the leading edge. Figure 12 shows the pressure drag is dominant among the total drag. Furthermore, Figure 13 suggests most of the difference in the total drag for each M corresponds to the difference in the pressure drag. From the above, it is observed that the pressure drag increases at $M = 0.60$ due to the increase in the separation region, resulting in a larger total drag than that at $M = 0.20$. Above $\alpha = 7^{\circ}$, the LSB disappears at $M = 0.60$ due to the compressibility effect as shown in Figure 15. According to Ref. [12], although the separated shear layer in incompressible flow is prone to transition from laminar to turbulent flow due to the Kelvin-Helmholtz (KH) instability, the KH instability of the separated shear layer is alleviated and stabilized by the compressibility effect as the M increases. Similarly, above $\alpha = 7^{\circ}$ at $M = 0.60$, it is considered that the separated shear layer stabilization due to the compressibility effect would have caused the reattachment point to pass over the trailing edge, resulting in the disappearance of the LSB.

3.2.2. Transonic Region

To evaluate the effects of shock waves on aerodynamic performance and the flow fields, the results from $M = 0.60$ to $M = 1.2$ are compared. The averaged density gradient fields between $M = 0.80$ and $M = 1.2$ are shown in Figure 17. It can be confirmed that shock waves are generated at all angles of attack at $M = 1.0$ and $M = 1.2$. A trailing edge shock wave is generated at $M = 1.0$ whereas a bow shock wave is observed in front of the leading edge at $M = 1.2$. These are very similar to typical flow fields around the airfoils under the Earth's atmosphere [27]. In contrast, multiple λ-type shock waves are generated over the separated shear layer at

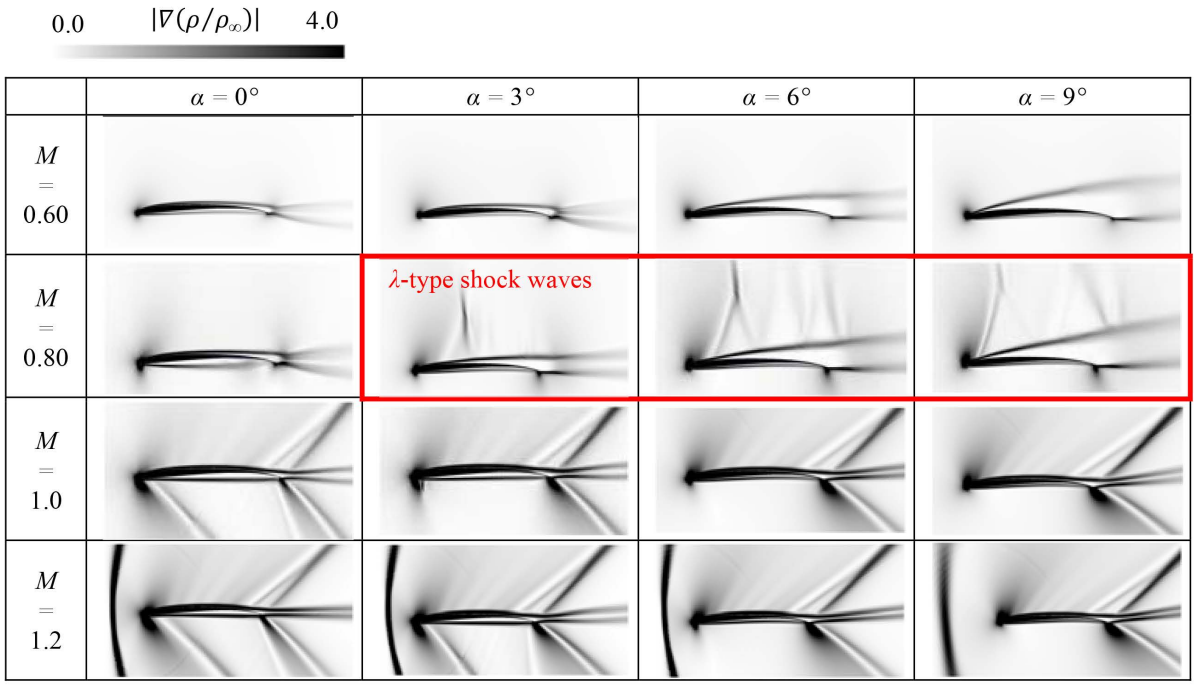

Figure 17. Comparison of density gradient around CLF5605 in the transonic region.

M = 0.80 above α = 3˚ which is interestingly very similar to the shock wave structure at Re = 200,000 reported by Drela [13]. Drela describes the multiple λ-type shock waves generation mechanism as follows. The precompression wave separates the boundary layer and collides with the separated shear layer. This causes the precompression to be reflected as an expansion wave. As a result, multiple λ-type shock waves are generated. It can be deduced that the multiple λ-type shock waves at Re = 15,400 are generated by a similar mechanism. The C_p distributions are shown in **Figure 18**.

From the results of the lift and drag coefficients of each M shown in **Figure 19** below α = 5˚, the C_l noticeably becomes smaller at higher M, especially M = 1.0 and M = 1.2. As shown in **Figure 18(a)** and **Figure 18(b)**, the pressure and suction sides become negative and positive pressure, respectively, upstream from around x/c = 0.4 or 0.2 above M = 1.0. Both of these pressures generate act on the airfoil in the opposite direction of the lift force. As a result, the C_l decreased at higher M. Although a similar pressure distribution is observed below M = 0.80, its effect is minimal because it occurs in a localized region upstream of x/c = 0.1. In contrast, above M = 0.80, the C_d increases compared to M = 0.60 at all angles of attack. However, the C_d at M = 1.0 exceeds that at M = 1.2. The C_{dp} at

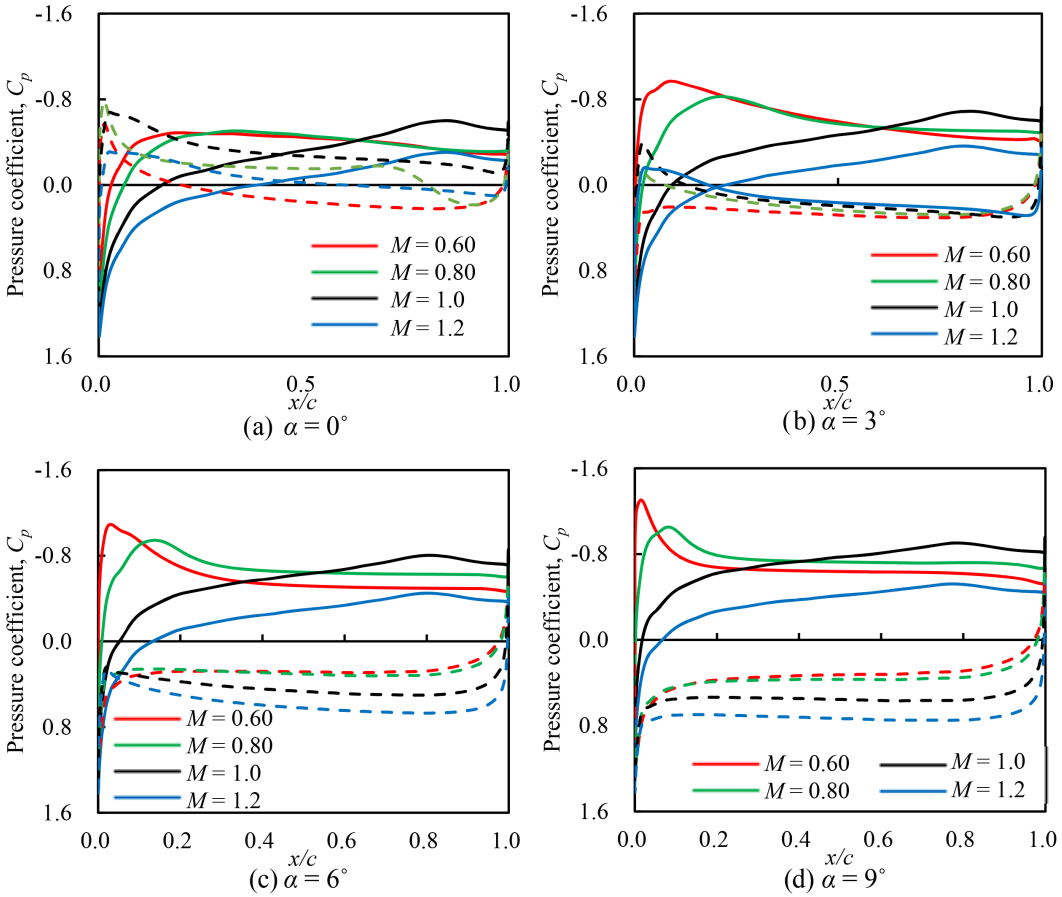

Figure 18. Comparison of C_p distribution between M = 0.60 and M = 1.2. (Solid line: suction side, Dashed line: pressure side).

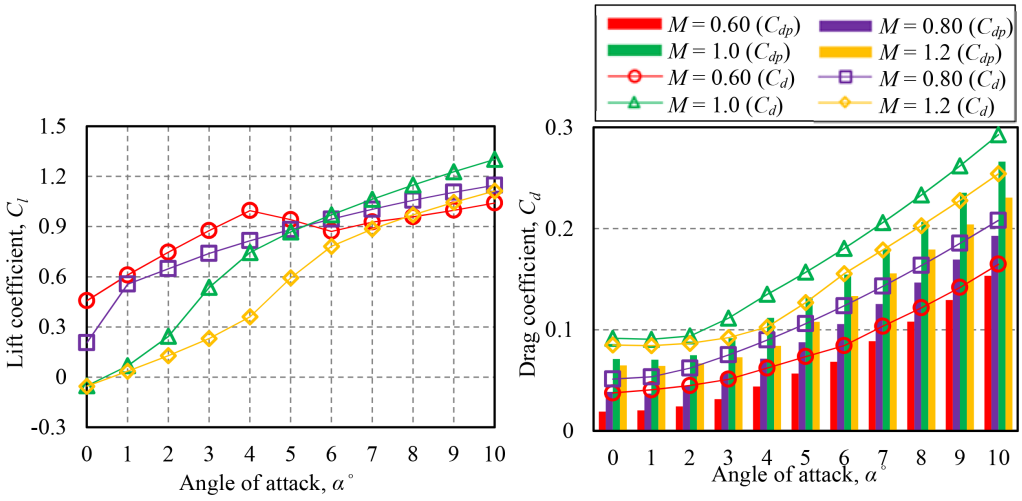

(a) Lift curve (b) Drag curve and pressure drag coefficients (C_{dp})

Figure 19. Comparison of aerodynamic coefficients between $M = 0.60$ and $M = 1.2$.

each M is also shown in Figure 19(b). In all cases, the C_{dp} is the main source of the total drag. As shown in Figure 18, especially at low angles of attack, the positive pressure near the leading edge on the suction surface acts on the airfoil as drag. On the other hand, focusing on the vicinity of the trailing edge, the negative pressure on the suction side near the trailing edge where the camber is large is the largest at $M = 1.0$, resulting in a larger drag at $M = 1.0$ than that at $M = 1.2$.

4. Conclusions

To investigate the MH rotor blade aerodynamic performance and the flow field under low-Reynolds compressible flows, two-dimensional unsteady simulations were performed using the CLF5605 airfoil. The M effects on the flow field and aerodynamic performance were evaluated.

The comparison of the results for $M = 0.20$ and $M = 0.60$ reveal that the LSB disappears above $\alpha = 7^\circ$ at $M = 0.60$ due to the KH instability stabilization in the separated shear layer by the compressibility effect. These phenomena have been reported in previous studies using other airfoils, and the same phenomenon was found in the present study. Above $\alpha = 3^\circ$ at $M = 0.80$, multiple λ-type shock waves are observed over the separated shear layer on the suction side. Furthermore, however, the effect of the separated shear layer is more dominant than the λ-type shock wave for the C_p distribution on the airfoil surface. For $M = 1.0$ and $M = 1.2$, due to the characteristic pressure distribution near the leading and trailing edges, the lift coefficients become much smaller than those for $M \leq 0.80$, especially at the low angles of attack below $\alpha = 5^\circ$, and the drag coefficients at $M = 1.0$ are maximum for all angles of attack.

Since technical difficulties remain in developing wind tunnels that rigorously achieve flow conditions for the MH, numerical simulations are expected to continue to be the main method for fluid analysis under such flow conditions. In numerical analysis, future issues include clarification of the three-dimensional

and unsteady nature of the flow field. Focusing on the flow conditions where the interference between the separated shear layer and shock waves was observed in this study, our research group is currently analyzing the three-dimensional flow field around the MH rotor and unsteadiness such as buffeting by applying higher-order accurate analyses such as large eddy simulation (LES) and DNS.

Acknowledgments

A part of this study was supported by the JSPS KAKEN Grant Number 22H01685. The computations were carried out using the computer resource offered under the category of general projects by the Research Institute for Information Technology, Kyushu University. The numerical calculations were performed using FaSTAR, a compressible fluid dynamics solver developed by JAXA.

Conflicts of Interest

The authors declare no conflicts of interest regarding the publication of this paper.

References

[1] Datta, A., *et al.* (2003) Design of a Martian Autonomous Rotary-Wing Vehicle. *Journal of Aircraft*, **40**, 461-472. https://doi.org/10.2514/2.3141

[2] Sugiura, M., *et al.* (2020) Aerodynamic Optimal Design of Mars Helicopter Rotor Blade Planform. *Proceedings of the FDCJANSS*, city, 28-30 September 2020, 157-164.

[3] Sato, M., *et al.* (2021) Mach Number Effects on Rotor Performance of Martian Helicopter "HAMILTON". *Proceedings of the FDCJANSS*, 30 June - 2 July 2021.

[4] Northon, K. (2021) NASA's Ingenuity Mars Helicopter Succeeds in Historic First Flight. https://www.nasa.gov/press-release/nasa-s-ingenuity-mars-helicopter-succeeds-in-historic-first-flight

[5] Koning, W.J.F., Johnson, W. and Allan, B.G. (2018) Generation of Mars Helicopter Rotor Model for Comprehensive Analyses. *Proceedings of the AHS International Technical Meeting on Aeromechanics Design for Transformative Vertical Flight*, San Francisco, 16-18 January 2018.

[6] Koning, W.J.F., Johnson, W. and Grip, H.F. (2019) Improved Mars Helicopter Aerodynamic Rotor Model for Comprehensive Analyses. *AIAA Journal*, **57**, 3969-3979. https://doi.org/10.2514/1.J058045

[7] Canuto, D. and Taira, K. (2015) Two-Dimensional Compressible Viscous Flow around a Circular Cylinder. *Journal of Fluid Mechanics*, **785**, 349-371. https://doi.org/10.1017/jfm.2015.635

[8] Takaki, R. (2006) Aerodynamic Characteristics of NACA4402 in Low Reynolds Number Flows. *Journal of the Japan Society for Aeronautical and Space Sciences*, **54**, 367-373. https://doi.org/10.2322/jjsass.54.367

[9] Suwa, T., Nose, K., Numata, D., Nagai, H. and Asai, K. (2012) Compressibility Effects on Airfoil Aerodynamics at Low Reynolds Number. 30*th AIAA Applied Aerodynamics Conference* 2012, New Orleans, 25-28 June 2012, 1571-1583. https://doi.org/10.2514/6.2012-3029

[10] Munday, P. M., Taira, K., Suwa, T., Numata, D. and Asai, K. (2015) Nonlinear Lift

on a Triangular Airfoil in Low-Reynolds-Number Compressible Flow. *Journal of Aircraft*, **52**, 924-931. https://doi.org/10.2514/1.C032983

[11] Anyoji, M., Numata, D., Nagai, H. and Asai, K. (2015) Effects of Mach Number and Specific Heat Ratio on Low-Reynolds-Number Airfoil Flows. *AIAA Journal*, **53**, 1640-1654. https://doi.org/10.2514/1.J053468

[12] Mukohara, H. and Anyoji, M. (2022) Computational Analysis of Compressibility Effect on Flow Field and Aerodynamics at Low Reynolds Numbers. *Physics of Fluids*, **34**, Article ID: 056109. https://doi.org/10.1063/5.0079186

[13] Drela, M. (1992) Transonic Low-Reynolds Number Airfoils. *Journal of Aircraft*, **29**, 1106-1113. https://doi.org/10.2514/3.46292

[14] McMasters, J.H. and Henderson, M.L. (1979) Low-Speed Single-Element Airfoil Synthesis. *Technical Soaring*, **6**, 1-31.

[15] Anyoji, M., *et al.* (2011) Development of a Low-Density Wind Tunnel for Simulating Martian Atmospheric Flight. *Transactions of the JSASS Aerospace Technology Japan*, **9**, 21-27. https://doi.org/10.2322/tastj.9.21

[16] Hashimoto, A., *et al.* (2015) Development of Fast Unstructured-Grid Flow Solver FaSTAR. *Journal of the Japan Society for Aeronautical and Space Sciences*, **63**, 96-105. https://doi.org/10.2322/jjsass.63.96

[17] Kitamura, K. and Shima, E. (2010) Improvements of Simple Low-Dissipation AUSM against Shock Instabilities in Consideration of Interfacial Speed of Sound. *Proceedings of the ECCOMAS CFD* 2010, Lisbon, 14-17 June 2010, Paper No. 1283.

[18] Winslow, J., Otsuka, H., Govindarajan, B. and Chopra, I. (2017) Basic Understanding of Airfoil Characteristics at Low Reynolds Numbers (10^4-10^5). *Journal of Aircraft*, **55**, 1050-1061. https://doi.org/10.2514/1.C034415

[19] Radespiel, R.E., Windte, J. and Scholz, U. (2007) Numerical and Experimental Flow Analysis of Moving Airfoils with Laminar Separation Bubbles. *AIAA Journal*, **45**, 1346-1356. https://doi.org/10.2514/1.25913

[20] Coder, J.G. and Maughmer, M.D. (2014) Computational Fluid Dynamics Compatible Transition Modeling Using an Amplification Factor Transport Equation. *AIAA Journal*, **52**, 2506-2512. https://doi.org/10.2514/1.J052905

[21] Menter, F.R. (1992) Improved Two-Equation k-omega Turbulence Models for Aerodynamic Flows. NASA TM 103975. https://doi.org/10.2514/6.1993-2906

[22] Langtry, R.B. and Menter, F.R. (2009) Correlation-Based Transition Modeling for Unstructured Parallelized Computational Fluid Dynamics Codes. *AIAA Journal*, **47**, 2894-2906. https://doi.org/10.2514/1.42362

[23] Menshov, O.S. and Nakamura, Y. (1995) Implementation of the LU-SGS Method for an Arbitrary Finite Volume Discretization. *Proceedings of the* 9*th Japan Conference on CFD*, Tokyo, 20-22 December 1995, 123-124.

[24] Shima, E., Kitamura, K. and Haga, T. (2013) Green-Gauss/Weighted-Least-Squares Hybrid Gradient Reconstruction for Arbitrary Polyhedra Unstructured Grids. *AIAA Journal*, **51**, 2740-2747. https://doi.org/10.2514/1.J052095

[25] Roe, P.L. (1986) Characteristic-Based Schemes for the Euler Equations. *Annual Review of Fluid Mechanics*, **18**, 337-365. https://doi.org/10.1146/annurev.fl.18.010186.002005

[26] Taniguchi, S., *et al.* (2020) Experimental and RANS Analysis of Full Mars Airplane Configurations. *AIAA Scitech* 2020 *Forum*, Orlando, 6-10 January 2020, 1-14. https://doi.org/10.2514/6.2020-2224

[27] Jacobs, E.N. (1936) Methods Employed in America for the Experimental Investigation of Aerodynamic Phenomena at High Speeds. Volta Meeting Paper, 42.

Nomenclature

α: Angle of attack, °
C_d: Drag coefficient
C_{dp}: Pressure drag coefficient
C_f: Skin-friction coefficient
C_l: Lift coefficient
C_p: Pressure coefficient
c: Airfoil chord length, m
M: Mach number
R: Rotor radius, m
Re: Reynolds number
r: Rotor radial coordinate, m
t: Real-time, s
u: Uniform flow velocity, m/s
x: Chordwise distance from the leading edge, m
y: Distance from the leading edge in the airfoil thickness direction, m
y^+: Dimensionless wall distance

Subscripts

tip: Blade tip
x: x direction
∞: Freestream conditions